PAPER

Neutral pathways and heat flux widths in vertical- and horizontal-target EDGE2D-EIRENE simulations of JET

To cite this article: D. Moulton *et al* 2018 *Nucl. Fusion* **58** 096029

IOP Publishing | International Atomic Energy Agency Nuclear Fusion

Nucl. Fusion **58** (2018) 096029 (12pp) https://doi.org/10.1088/1741-4326/aacf0f

Neutral pathways and heat flux widths in vertical- and horizontal-target EDGE2D-EIRENE simulations of JET

D. Moulton[1], G. Corrigan[1], J.R. Harrison[1], B. Lipschultz[2] and JET Contributors[a]

EUROfusion Consortium, JET, Culham Science Centre, Abingdon OX14 3DB, United Kingdom of Great Britain and Northern Ireland

[1] UKAEA-CCFE, Culham Science Centre, Abingdon, OX14 3DB, United Kingdom of Great Britain and Northern Ireland

[2] Department of Physics, University of York, Heslington, York, YO10 5DD, United Kingdom of Great Britain and Northern Ireland

E-mail: david.moulton@ukaea.uk

Received 28 March 2018, revised 11 June 2018
Accepted for publication 26 June 2018
Published 12 July 2018

Abstract

This paper further analyses the EDGE2D-EIRENE simulations presented by Chankin *et al* (2017 *Nucl. Mater. Energy* **12** 273), of L-mode JET plasmas in vertical–vertical (VV) and Vertical–horizontal (VH) divertor configurations. As expected, the simulated outer divertor ionisation source peaks near the separatrix in VV and radially further out in VH. We identify the reflections of recycled neutrals from lower divertor tiles as the primary mechanism by which ionisation is concentrated on the outer divertor separatrix in the VV configuration. These lower tile reflection pathways (of neutrals from the outer divertor, and to an even greater extent from the inner divertor) dominate the outer divertor separatrix ionisation. In contrast, the lower-tile-reflection pathways are much weaker in the VH simulation and its outer divertor ionisation is dominated by neutrals which do not reflect from any surfaces. Interestingly, these differences in neutral pathways give rise to strong differences in the heat flux density width λ_q at the outer divertor entrance: $\lambda_q = 3.2$ mm in VH compared to $\lambda_q = 11.8$ mm in VV. In VH, a narrow channel exists in the near scrape-off-layer (SOL) where the convected heat flux, driven by strong $E_r \times B$ flow and thermoelectric current, dominates over the conducted heat flux. The width of this channel sets λ_q and is determined by the radial distance between the separatrix and the ionisation peak in the outer divertor.

Keywords: neutral pathways, divertor configuration, heat flux width, EDGE2D-EIRENE

(Some figures may appear in colour only in the online journal)

1. Introduction

1.1. Overview

It is well known that horizontal- and vertical-target diverted plasmas perform differently, in terms of divertor target profiles, detachment onset and particle throughput. The reader is referred to [10] and references therein for a thorough review of these effects, and to [9] for the impact of divertor geometry on particle throughput. More recently, it has become apparent that the L-H power threshold is significantly lower in horizontal-target configurations than in vertical-target configurations (e.g. [11]). Our understanding of the underlying neutral pathways that ultimately give rise to these differences appears somewhat lacking, however.

Here, in an attempt to ellucidate these neutral pathways, we further analyse the EDGE2D-EIRENE [12, 14, 15] simulations presented by [1]. These are of two L-mode experiments

[a] See the author list of Litaudon [16].

on JET, in vertical–vertical (VV; vertical inner target, vertical outer target) and Vertical–horizontal (VH; vertical inner target, horizontal outer target) divertor configurations. This analysis will be presented in section 2. In the course of this analysis, we noticed the rather interesting effect that the heat flux density profile at the outer divertor entrance is significantly narrower and more peaked in the VH simulation than in the VV simulation. This will be presented in section 3. Finally in sections 4 and 5 we discuss and conclude.

1.2. Recap of the simulations analysed here

Figures 1(*a*) and (*b*) show the VV and VH EDGE2D grids used for the two JET simulations taken from [1]. The separatrices are shown in magenta and the divertor entrances are in green. As indicated by the axes colours, VV results will be plotted in blue and VH results will be plotted in red throughout this paper. The VV simulation corresponds approximately to pulse 84 727 at 57.7 s and the VH simulation corresponds approximately to pulse 81 883 at 57.0 s[3].

A full description of the two simulations has already been provided by [1]. To recap, the main input parameters are as follows:

(i) The same input heating power (shared equally between electrons and ions) of 3.6 MW in both cases, to match experimental power balance[4].
(ii) The same plasma current of 2.0 MA in both cases.
(iii) The same toroidal magnetic field of 2.4 T at the magnetic axis in both cases.
(iv) Similar outer midplane separatrix electron densities of 1.0×10^{-19} m^{-3} for the VV case and 1.2×10^{-19} m^{-3} for the VH case.
(v) The same L-mode radial transport coefficients in both cases ($D_\perp = 1$ m^2 s^{-1} everywhere, $\chi_i = 2$ m^2 s^{-1} everywhere, $\chi_e = 0.5$ m^2 s^{-1} in the main scrape-off layer (SOL) and $\chi_e = 1$ m^2 s^{-1} everywhere else).
(vi) All drift and current terms turned on. Both simulations are in forward field i.e. the ion ∇B drift is downwards.

The comparison between simulation and experiment for the target probe data was shown in [1]. The agreement is not perfect (in particular for the outer target J_{sat} in the VH simulation), possibly due to the fact that the radial transport is kept constant between the two simulations. As was implicitly assumed in that paper, we assume here that despite this disagreement, by studying these two simulations we can still learn something (at least qualitatively) about vertical and horizontal divertor geometries even if, in reality, there is additional physics (such as changing radial transport) which has not been included here. It should be noted that the assumed diffusivities in the PFR ($D_\perp = \chi_e = 1$ m^2 s^{-1}, $\chi_i = 2$ m^2 s^{-1}) resulted in a heat flux profile at the outer target of the VH simulation with a fitted 'S/f_x' parameter of 0.6, in line with previous JET experiments (see figure 9 of [13]).

A key motivating factor for this paper was to understand the different outer target electron temperature ($T_{et,out}$) profiles in the VV and VH simulations. A zoomed-in view of these (mapped to the outer midplane) is given in figure 1(*c*) (note that the full radial extent of the grids mapped to the outer midplane is −1.5 cm to 4.7 cm for the VV simulation and −0.8 cm to 3.6 cm for the VH simulation). For VH, $T_{et,out}$ is radially decreasing throughout the SOL whereas, for VV, $T_{et,out}$ is radially increasing in the near SOL.

As described in [1], the opposite radial gradient signs in the near SOL $T_{et,out}$ result in opposite signs in the near SOL radial electric field at the outer midplane; the potential at the outer target sheath entrance, approximated by $V_{se} \sim -3k_B T_{et,out}/e$, extends all the way up to the outer midplane. This is demonstrated in figure 1(*d*), where we plot the radial electric field at the outer midplane ($E_{r,OMP}$) for VV and VH simulations (solid lines), alongside the radial gradient in $-(3k_B/e)T_{et,out}$ mapped to the outer midplane (dashed lines). In both VV and VH, $E_{r,OMP}$ is quite well described by $-(3k_B/e)\partial T_{et,out}/\partial R_{OMP}$. It was speculated in [1] that the larger shear in $E_{r,OMP}$ near the separatrix in VH might be why the VH configuration has a lower power threshold for L-H transition compared to VV. Figure 1(*d*) suggests that in order to understand this effect, we need to understand the difference in $T_{et,out}$ profiles in the two simulations.

1.3. The target electron temperature in terms of particle and heat balance

Using the target heat flux boundary condition in combination with particle and heat balance equations, and ignoring (generally small) contributions from non-orthogonal fluxes, we find the following expression for the target electron temperature:

$$T_{et} = \frac{q_{\theta u}(B_u/B_{\theta u}) + \frac{1}{dA_{\parallel u}} \int_t^u S_q dV}{\gamma \left(\Gamma_{i\theta u}(B_u/B_{\theta u}) + \frac{1}{dA_{\parallel u}} \int_t^u S_i dV \right)}. \quad (1)$$

Here, subscripts 'u' and 't' denote values at the divertor entrance end and at the target end, respectively, of the flux tube under consideration; q_θ is the total poloidal heat flux density; B is the total magnetic field strength; B_θ is the poloidal magnetic field strength; $dA_\parallel$ is the elementary area normal to the magnetic field; S_q is the total heat source density (including the difference between radial fluxes into and out of the flux tube); dV is the elementary volume along a flux tube; $\Gamma_{i\theta}$ is the total poloidal ion particle flux density; S_i is the total ion particle source density (including the difference between radial fluxes into and out of the flux tube[5]). The effective sheath heat transmission coefficient is given by $\gamma = \frac{T_{it}}{T_{et}}\gamma_i + \frac{\Gamma_{e\theta t}}{\Gamma_{i\theta t}}\gamma_e$, where T_i is the ion temperature; $\Gamma_{e\theta}$ is the ion poloidal particle flux density; γ_e and γ_i are the electron and ion sheath heat transmission coefficients (here we use $\gamma_i = 2.5$ and $\gamma_e = 4.5$ as a code input).

[3] The simulations from [1] were rerun to convergence with the latest version of EDGE2D-EIRENE and, consequently, results presented in this paper may differ slightly from those in that original paper. The effect on the solutions was found to be small, however.
[4] In [1] the input power is stated as 2.7 MW but this is a typographical error.
[5] In equation (1), both S_i and S_q are integrated over the entire volume of the flux tube, from target to divertor entrance.

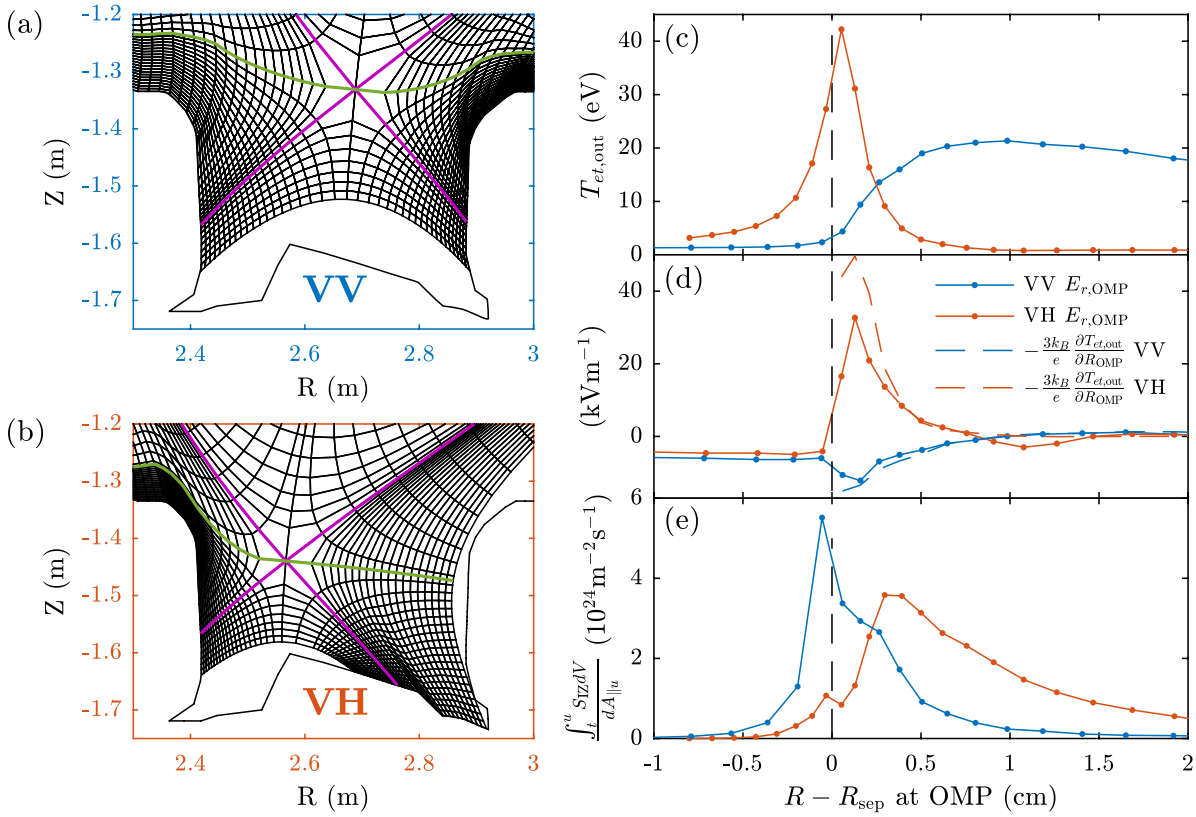

Figure 1. Overview of the two simulations analysed here. (*a*) and (*b*) The EDGE2D plasma grids for (*a*) the VV simulation and (*b*) the VH simulation. (*c*) The outer target electron temperature as a function of the major radius at the outer midplane. (*d*) The radial electric field at the outer midplane, compared to the radial gradient in the outer target electron temperature. (*e*) The flux-tube-integrated ionisation source in the outer divertor (divided by the parallel area at the divertor entrance for consistency with equation (1)).

Equation (1) states that the T_{et} at the target-end of a flux tube decreases with decreasing heat flux into the divertor-entrance-end of the flux tube, as well as with increasing heat sink along the flux tube. Also, T_{et} decreases with increasing particle flux into the divertor and with increasing particle source in the divertor. Physically, an increased divertor particle source leads to an increased target particle flux so that, in order to maintain power balance, the target temperature must decrease. In both VV and VH simulations, ionisation is the dominant particle source over both recombination (which is negligible) and also the divergence of the radial particle flux.

The flux-tube-integrated ionisation source in the outer divertor (divided by $\mathrm{d}A_{\|u}$ for consistency with (1)), is plotted in figure 1(*e*). In line with the above reasoning, we see that $T_{\mathrm{et,out}}$ is low in regions where the flux-tube-integrated ionisation is high, i.e. at the separatrix in VV and radially outward from the separatrix in VH. Note also that, in the VH simulation, $T_{\mathrm{et,out}}$ drops over a gradient length set by the radial distance between the separatrix and the position of the flux-tube-integrated ionisation source's peak. As will be seen in section 3, this in turn sets the width of a narrow heat convection region (driven by strong poloidal $E_r \times B$ and thermoelectric flows) which actually sets λ_q at the outer divertor entrance of the VH simulation, and leads to λ_q being 3.7 times narrower in VH than in VV. Before presenting this interesting phenomenon, however, we analyse the neutral pathways that give rise to the difference in the peak ionisation location.

2. The neutral pathways responsible for the divertor ionisation sources

2.1. vertical–vertical simulation

Figure 2 shows the neutral pathways comprising the divertor ionisation source for the VV simulation. In figure 2(*a*), we plot a schematic of the neutral pathways considered for the inner divertor ionisation. Directly below, in figure 2(*c*), we plot the components of $\int_t^u S_{\mathrm{IZ}}\mathrm{d}V/\mathrm{d}A_{\|}$ in the inner divertor (grey region in figure 2(*a*)), due to each of these pathways. Likewise, in figure 2(*b*), we plot a schematic of the neutral pathways considered for the outer divertor ionisation, while in figure 2(*d*) we plot the components of $\int_t^u S_{\mathrm{IZ}}\mathrm{d}V/\mathrm{d}A_{\|}$ in the outer divertor (grey region in figure 2(*b*)) due to each of those pathways. Note again that the total outer divertor flux-tube-integrated ionisation profile peaks at the separatrix.

The pathways considered are: (i) neutrals that originate from outer target recycling and have no contact with the lower tiles before ionising (light blue); (ii) neutrals that originate from outer target recycling and undergo at least one reflection from the lower tiles (dark blue); (iii) neutrals that originate from inner target recycling and have no contact with the lower tiles before ionising (light red); (iv) neutrals that originate from inner target recycling and undergo at least one reflection from the lower tiles (dark red). In figures 2(*c*) and (*d*) we also consider neutrals that originate from other (non-target)

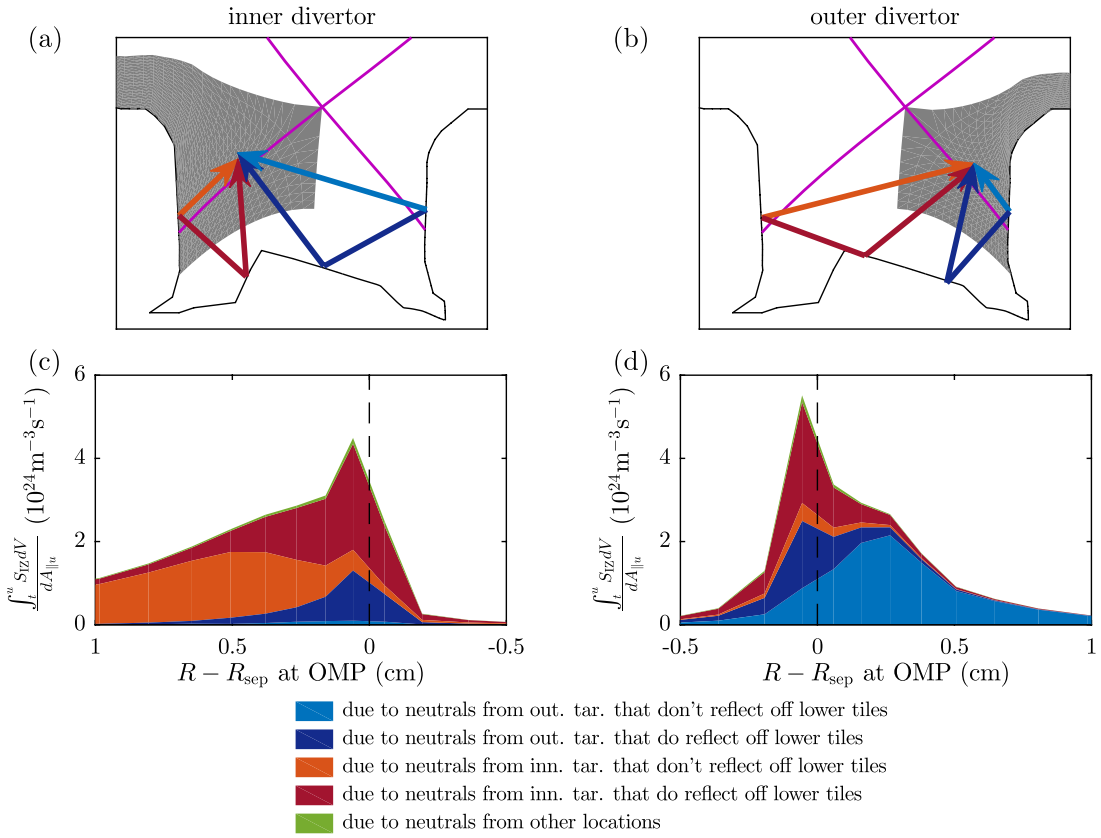

Figure 2. The neutral pathways comprising the inner divertor (left-hand side) and outer divertor (right-hand side) ionisation source for the VV simulation. (*a*) and (*b*) Show schematic representations of the neutral pathways considered, (*c*) and (*d*) show the components of the total ionisation due to each pathway. See text for details.

locations (green blocks; this includes neutrals originating from volumetric recombination), but we see that these do not contribute significantly to the divertor ionisation.

The first thing to note from figure 2 is that the private flux region (PFR) is sufficiently transparent to neutrals that *most of the ionisation that occurs along the separatrix is due to neutrals that reflect off the lower tiles*. 63% of the ionisation along the outer separatrix is due to neutrals that undergo at least one reflection off the lower tiles (the sum of dark red and dark blue blocks in figure 2(*d*) at the separatrix), while 84% of the ionisation along the inner separatrix is due to neutrals that undergo at least one reflection off the lower tiles. Furthermore, in the PFR and up to the near SOL, there is a strong exchange of neutrals between the divertors. Focussing on the outer divertor, of all the ionisation along the the outer separatrix, 44% is due to neutrals that originate from the inner target (the sum of light and dark red blocks in figure 2(*d*) at the separatrix). Most (83%) of this contribution from the inner target is due to lower-tile-reflected neutrals.

We do not believe that the importance of these lower tile reflection pathways (from both inner and outer targets) have been previously recognised, in regard to them causing the outer divertor ionisation to peak at the separatrix in a VV divertor configuration. A more detailed analysis of these lower tile reflection pathways is therefore appropriate.

2.2. More detailed analysis of the lower tile reflection pathways

Figure 3(*a*) (left axis) shows the cumulative ionisation source along the outer divertor separatrix, cumulated as a function of the position along the inner target from which lower-tile-reflected neutrals originate. The value of this blue curve at maximum radial distance is the total contribution to $\int_t^u S_{IZ}\mathrm{d}V/\mathrm{d}A_{\|u}$ along the outer target separatrix due to all lower-tile-reflected inner target neutrals (i.e. the height of the dark red patch at the separatrix in figure 2(*d*)). Overplotted on the right axis of figure 3(*a*) is the inner target electron temperature. Figure 3(*b*) shows the same plots for neutrals originating from the outer target; the value of this blue curve at maximum radial distance in figure 3(*b*) is the height of the dark blue patch at the separatrix in figure 2(*d*).

We see from these plots that lower-tile-reflected neutrals from the inner target contribute 42% more to the outer divertor separatrix ionisation than lower-tile-reflected neutrals from the outer target. Furthermore, the majority of neutrals that reflect off lower tiles and penetrate to the outer divertor separatrix originate from regions where the target electron temperature is below 5 eV. This is true of neutrals from both targets.

Figures 3(*c*) and (*d*) again show the ionisation source along the outer divertor separatrix due to lower-tile-reflected neutrals originating from the inner and outer target, respectively. Now,

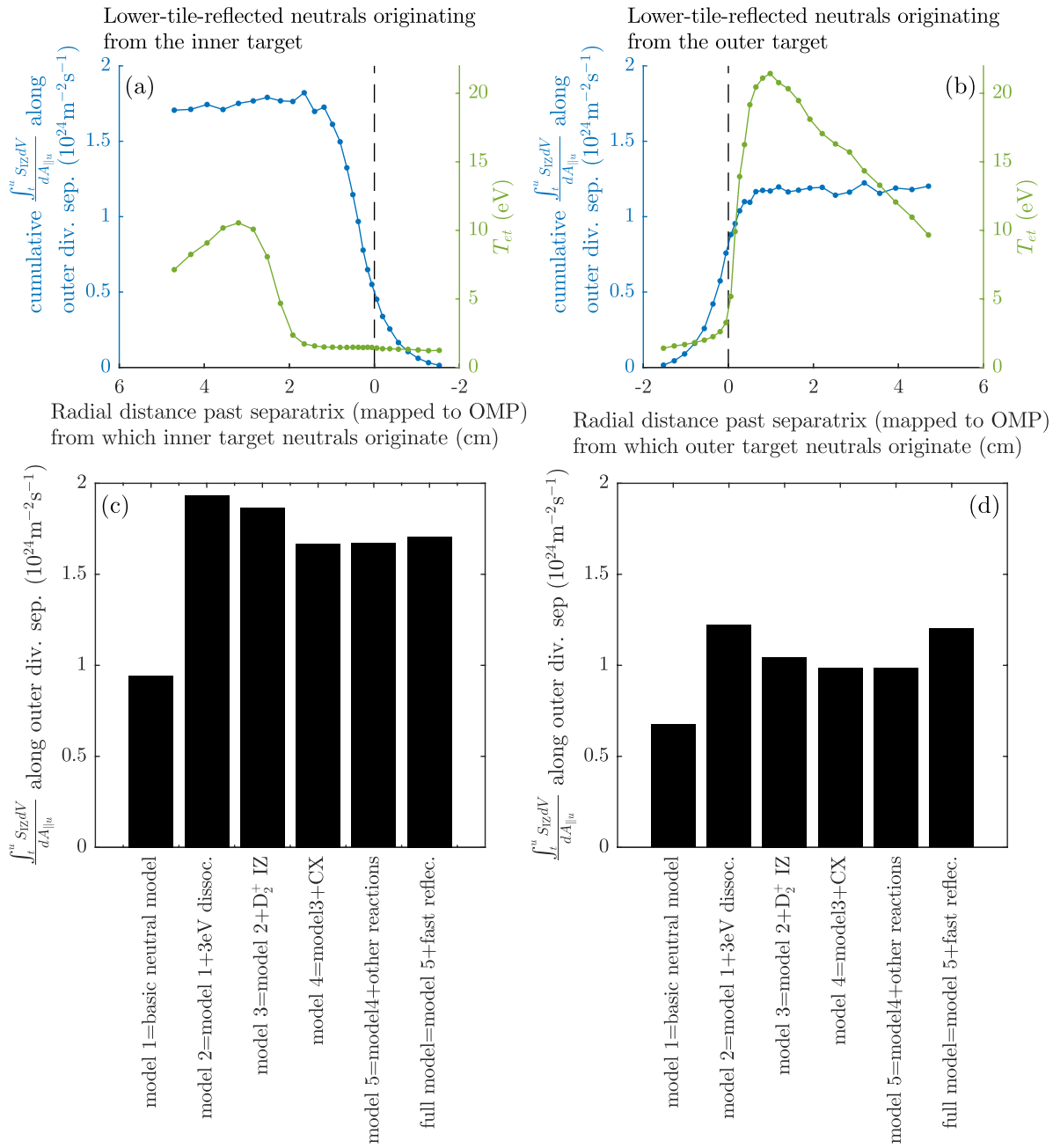

Figure 3. (*a*) and (*b*) Radial origin of neutrals which reflect from lower tiles and contribute to the outer divertor separatrix ionisation source, with the target electron temperature overlaid. (*c*) and (*d*) The outer divertor separatrix ionisation source due to lower-tile-reflected neutrals from the inner target (*c*) and from the outer target (*d*), as a function of increasingly complex neutral models. See text for details.

values are given as a function of increasingly complex neutral models. The intention here is to find the minimally complex neutral model that reproduces the outer divertor separatrix ionisation source for the full neutral model (i.e. the value of the rightmost bar). Each of these models was only run for a single (time-independent, 'standalone') EIRENE calculation, on the same background plasma. The 'basic model' referred to in the leftmost bar labels of figures 3(*c*) and (*d*) has the following properties:

(i) The targets and lower tiles have a temperature of 300 °C. All impinging D^+ ions are recycled as thermal D_2 molecules; no fast (atomic) reflections are allowed from either targets or lower tiles.

(ii) Only basic molecular dissociation ($D_2 + e \rightarrow 2D + e$) and atomic ionisation ($D + e \rightarrow D^+ + 2e$) are allowed.

(iii) After a dissociation event practically no energy is passed to either atom (molecules can still dissociate but the velocity of the resulting atoms is sufficiently low that their ionisation mean-free paths are negligibly small).

Interestingly, just with this basic model where the highest energy that any neutral can obtain is their 0.07 eV desorption energy, a significant fraction of the total lower-tile-reflection pathway (observed with the full neutral model) is activated. That is, the *dissociation* path length of thermally desorbed molecules in the PFR is similar to the width of the PFR. This

Table 1. Overview of the models used to understand the mechanisms by which neutrals are able to recycle from the targets, reflect off the lower tiles and penetrate back to the separatrix before ionising.

		Model number					
		1	2	3	4	5	6
Ionisation	$D + e \rightarrow D^+ + 2e$	✓	✓	✓	✓	✓	✓
Dissociation	$D_2 + e \rightarrow 2D + e$	✓	✓	✓	✓	✓	✓
Target and lower tile temperatures		300 K	300 °C	300 °C	300 °C	300 °C	300 °C
Energy passed to dissociated atoms (each)		0 eV	3 eV	3 eV	3 eV	3 eV	3 eV
Non-dissociative ionisation	$D_2 + e \rightarrow D_2^+ + 2e$	✗	✗	✓	✓	✓	✓
Dissociative excitation	$D_2^+ + e \rightarrow D + D^+ + e$	✗	✗	✓	✓	✓	✓
Dissociative D_2^+ ionisation	$D_2^+ + e \rightarrow 2D^+ + 2e$	✗	✗	✓	✓	✓	✓
Charge exchange	$D + D^+ \rightarrow D^+ + D$	✗	✗	✗	✓	✓	✓
Dissociative D_2 ionisation	$D_2 + e \rightarrow D + D^+ + 2e$	✗	✗	✗	✗	✓	✓
Dissociative recombination	$D_2^+ + e \rightarrow 2D$	✗	✗	✗	✗	✓	✓
Fast reflections from TRIM database		✗	✗	✗	✗	✗	✓

is consistent with the observation that most of the lower-tile-reflection pathway is constructed from neutrals that originate from target positions where the electron temperature is below 5 eV, where the dissociation rate is sufficiently low to allow thermally desorbed neutrals to reflect from lower tiles and penetrate to the outer divertor separatrix.

In model 2 we provide the default 3 eV to both atoms after a molecular dissocation event. Since atoms, in addition to non-dissociated molecules, can now escape the PFR, this acts to increase the total number of neutrals that reach and reflect off the lower tiles. Furthermore, those atoms can penetrate slightly further back into the SOL than the thermally desorbed molecules. Thus, there is a larger ionisation source at the separatrix in this case. In model 3 we include an additional ionisation path via non-dissociative ionisation of D_2, followed by dissociative excitation or ionisation of the resulting D_2^+ molecule (see table 1). This acts to slightly reduce the outer divertor separatrix ionisation due to lower-tile-reflected neutrals because there is more chance of the neutral ionising before it reaches the lower tiles. The reduction is slightly greater for neutrals from the outer target than for neutrals from the inner target.

In model 4 we include charge exchange between D atoms and D^+ ions. This again results in a slight reduction in the lower-tile-reflected outer divertor separatrix ionisation because the average path length to the lower tiles is increased. In model 5 we include the other neutral reactions in table 1, which have a negligible effect on the lower tile reflection pathway. Finally, in model 6, we allow fast reflections to take place from all surfaces (with a probability, calculated by the TRIM database [4], of 71% for the outer target and 77% for the inner target). Model 6 is then the same one as in the steady-state simulation. Interestingly, including fast reflections results in only a mild increase in the lower-tile-reflected outer divertor separatrix ionisation from outer target neutrals, and very little increase from inner target neutrals. Overall, the lower-tile reflection pathways (from both targets to the outer divertor separatrix) are mostly accounted for by the basic neutral model with realistic dissocation energy (i.e. model 3). A summary of the different models is given in table 1.

Given the high proportion of neutrals that are fast-reflected from both tiles, it is perhaps surprising to note the minimal effect that these have on the ionisation source calculated by EIRENE in standalone mode. This can be explained firstly because the fast-reflected neutrals are actually not that much faster (1.8 times, on average) than 3 eV dissociated atoms. Secondly, this increased speed is offset by the fact that fast-reflected neutrals only need to be ionised to stop them, whereas molecules need to be both dissociated and ionised.

2.3. Effect of removing neutrals that reflect off lower tiles and penetrate back to the outer divertor separatrix

The above analysis suggests an important role for neutrals reflected from the lower tiles in setting the VV divertor ionisation pattern. In order to confirm this, we created a VV simulation in which neutrals that reflect from the lower tiles are removed from the simulation (without contributing to the ionisation source) when (and only when) they reach back to the outer divertor separatrix. The resulting outer target T_{et}, outer midplane E_r and flux-tube-integrated ionisation source are shown in figure 4 (green lines). These are shown alongside the default VV and VH simulations already presented in figure 1.

We observe that the separatrix ionisation is significantly reduced by removing this pathway, to levels similar to the VH simulation. Consistent with this, $T_{et,out}$ is increased at the separatrix to values similar to those in VH, and $E_{r,OMP}$ becomes positive across the outer midplane SOL. Note that by removing (i.e. pumping) neutrals when they reach the separatrix, we provide little opportunity for ionisation radially outward from the separatrix; this is a particular feature of the horizontal configuration where neutrals are recycled into the SOL with a mean-free-path length shorter than the SOL width. Consistent with this, $T_{et,out}$ does not drop off radially as sharply as it does in the VH case and, therefore, $E_{r,OMP}$ has a lower magnitude.

2.4. Vertical–horizontal simulation

Figure 5 shows the same plots as in figure 2, but for the VH simulation. We now include an additional pathway (plotted

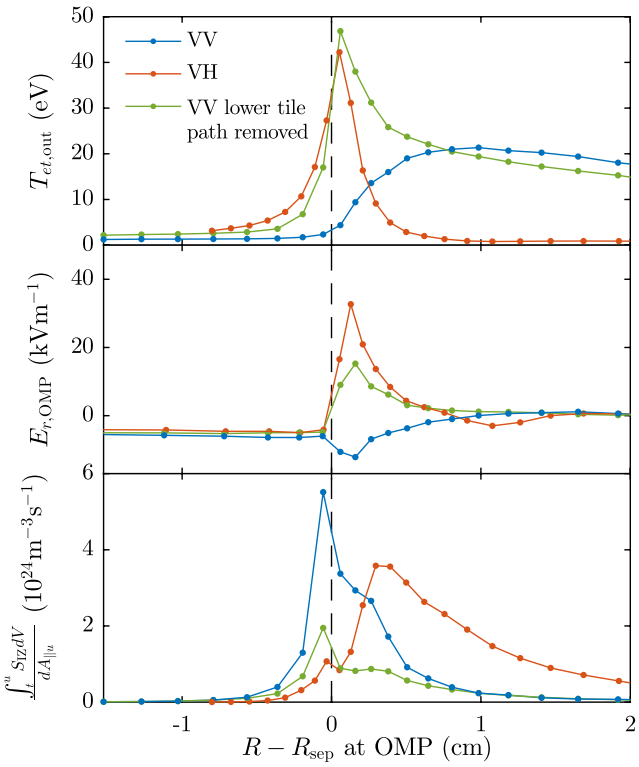

Figure 4. Effect of removing neutrals that reflect off the lower tiles from the VV simulation (green lines). The default VV and VH simulations are shown for reference.

in magenta) for neutrals from the outer target which reflect off the outer tiles of the simulation. Compared to the VV simulation, in which the outer divertor flux-tube-integrated ionisation profile peaks at the separatrix, the ionisation profile in figure 5(*d*) is observed to peak radially outward from the separatrix.

In contrast to the VV simulation, the peak outer divertor ionisation in the VH simulation is comprised almost entirely of neutrals from the outer target that ionise without any reflections, from either the lower or outer tiles. The orientation of the outer target is such that lower-tile-reflected neutrals originating from the outer target are negligible, while the relatively short ionisation mean free path of the SOL means that outer-tile-reflected neutrals do not contribute significantly either. There is some contribution to the outer divertor separatrix ionisation due to neutrals that originate from the inner target, but this contribution is a factor 4.6 lower than in VV. In part, this is due to a lower total inner target recycling flux in VH (1.5 times lower than in VV), caused by the lack of contribution to the inner target ionisation from the outer target neutrals (as evidenced in figure 5(*c*). Mostly, however, the inner target contribution is reduced because the PFR is hotter in the VH simulation so that neutrals cannot traverse across it so easily.

3. Heat balance in the divertor

The heat flux density deposited on a toroidally symmetric target is given by

$$q_{\mathrm{dep}} = \left(q_{\theta u}(B_u/B_{\theta u}) + \frac{1}{\mathrm{d}A_{\|u}} \int_t^u S_q \mathrm{d}V \right) \frac{1}{f_R} \cos\phi, \quad (2)$$

where $f_R \equiv B_u/B_t$ is the total flux expansion from divertor entrance to target and ϕ is the angle of incidence of the field line on the target. In the presence of cross-field drifts, binormal convective heat fluxes mean that $q_\theta(B/B_\theta) \neq q_{\|}$. It is therefore important to consider $q_{\theta u}(B_u/B_{\theta u})$ in our simulations, not just $q_{\|u}$; this $q_{\theta u}(B_u/B_{\theta u})$ is the heat flux density that the divertor is required to exhaust and $q_{\|u}$ does not contain all of it. From (2), $q_{\theta u}(B_u/B_{\theta u})$ can be reduced via heat sinks along the flux tube (including the radial divergence of the radial flows), total flux expansion and/or target incidence angle.

3.1. Heat flux profiles at the divertor entrance

Figures 6(*a*) and (*b*) show $q_{\theta u}(B_u/B_{\theta u})$ into the inner and outer divertor entrances, respectively (i.e. along the green lines in figures 1(*a*) and (*b*)). These are for the default simulations, in which drifts and parallel current are turned on (VV in blue and VH in red). Figures 6(*c*) and (*d*) show the same plots for a steady-state simulation in the absence of drifts, but still with parallel current turned on. Figures 6(*e*) and (*f*) again show the same plots for a steady-state simulation but now in the absence of both drifts and current. For ease of presentation, only the first 1.5 cm of SOL is shown, as a function of the radial distance mapped to the outer mid-plane. For both divertors, fluxes are defined to be positive going into the divertor.

Consider first the total power asymmetry between the outer and inner divertors (i.e. the surface integrals at the divertor entrance of the quantities plotted in figure 6). In line with previous results [2, 3], the outer-to-inner power asymmetry into the divertor entrances increases as a result of parallel current and drifts. In VV the ratio increases from 1.7:1 in the absence of both to 4.0:1 in the presence of both. In VH the ratio increases from 1.2:1 in the absence of both to 2.5:1 in the presence of both. Thus, for both VV and VH, drifts and current act to increase the total power to the outer divertor entrance while decreasing the total power to the inner divertor entrance. This happens primarily as a result of $E_r \times B$ flows which point towards the outer divertor across the majority of the SOL in both VV and VH configurations (but not all of it in VV, as will be discussed below).

It is important to note that the divertor does not actually need to safely exhaust divertor-entrance-integrated heat fluxes, measured in MW. Rather, it needs to safely exhaust the maximum heat flux *density* $q_{\theta u}(B_u/B_{\theta u})$, measured in MWm^{-2}. In this regard, the effect of drifts and current on the maximum (i.e. near-SOL) heat flux density differs greatly in VV compared to VH simulations. This is clearly demonstrated in figures 6(*b*), (*d*) and (*f*). In the presence of drifts and current, the maximum $q_{\theta u}(B_u/B_{\theta u})$ at the outer divertor entrance is 2.2 times larger in VH than in VV. Turning drifts off, that factor reduces to 1.5. Turning off parallel current as well, the peak $q_{\theta u}(B_u/B_{\theta u})$ are almost the same in both configurations. Furthermore, in the presence of drifts and current, the width of the outer divertor

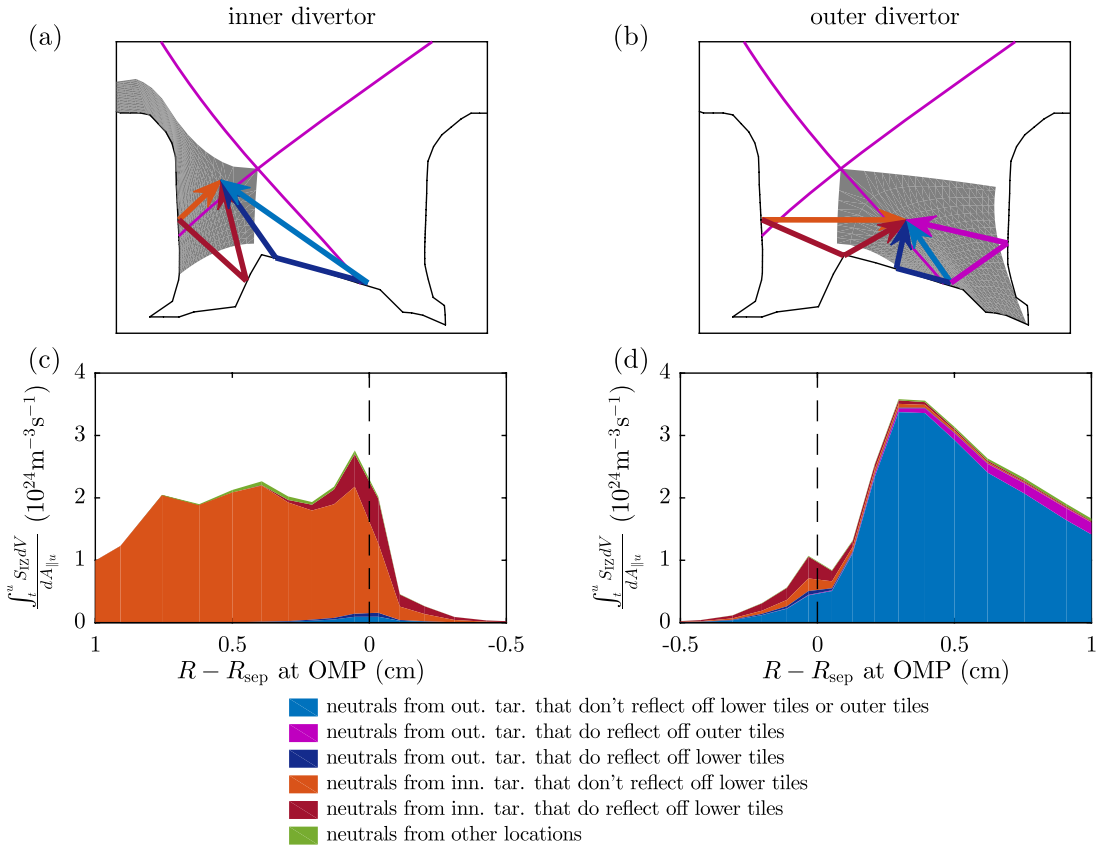

Figure 5. The neutral pathways comprising the divertor ionisation source for the VH simulation. Plots are the same as for figure 2 but with an extra neutral pathway considered due to outer-tile-reflected neutrals (plotted in magenta).

entrance heat flux profile λ_q (calculated by fitting an exponential to the data in figures 6(*b*), (*d*) and (*f*) and taking the e-folding length of that fit) is 3.7 times narrower in VH than in VV. In the absence of drifts and current this factor drops to 1.4. Recall that the radial transport coefficients were identical in the VV and VH simulations. These current- and drift-driven differences in the heat flux density profiles at the divertor entrances can therefore be attributed to the simulation geometry alone.

To assess the origin of these differences, we plot the components of $q_{\theta u}(B_u/B_{\theta u})$ at the outer divertor entrance in figure 7, for the default simulations with drifts and parallel current. The first thing to note from figure 7(*a*) is that the conducted heat flux densities into the outer divertor are quite similar in VV and VH simulations. In both cases, electron conduction dominates over ion conduction, and in fact the near-SOL electron conducted flux is actually slightly higher for VV than for VH. In the VV simulation, however, near-SOL poloidal $E_r \times B$ convective fluxes (figure 7(*b*)) point away from the outer target and act to attenuate this near-SOL conducted flux (in VV configuration the near-SOL E_r is negative because of the radially increasing target T_e).

By contrast, in the VH simulation, near-SOL $E_r \times B$ flux points towards the outer target and acts to enhance the near-SOL conducted heat flux (in VH configuration the near-SOL E_r is positive because of the radially decreasing target T_e). In addition, in VH, there is a strong near-SOL thermoelectric parallel current from the (higher T_e) outer target to the (lower T_e) inner target. This drives a convective parallel electron heat flux towards the outer divertor (figure 7(*c*)) and acts to further enhance the near-SOL $q_{\theta u}(B_u/B_{\theta u})$.

3.2. Outer divertor heat sinks and target heat flux densities

Figure 8(*a*) shows the total flux-tube-integrated heat source in the outer divertor for VV (blue) and VH (red) simulations, as a function of radial distance mapped to the outer midplane. These are normalised to the parallel area at the divertor entrance and are precisely the $\frac{1}{\mathrm{d}A_{\|u}} \int_t^u S_q \mathrm{d}V$ in equation (2). Negative values correspond to a heat sink. Figures 8(*b*)–(*e*) show the components of this source due to: (b) plasma-neutral interactions; (c) the radial divergence of the radial conducted heat flow; (d) the radial divergence of the radial anomalous-convected heat flow; (e) the radial divergence of the radial drift-convected heat flow. The blue lines in figures 8(*b*)–(*e*) sum to give the blue line in figure 8(*a*) and the red lines in figures 8(*b*)–(*e*) sum to give the red line in figure 8(*a*).

We observe that, in these relatively low density simulations, the outer divertor heat sink is dominated by the radial divergence of the radial flows. Losses due to plasma-neutral interactions (figure 8(*b*) are negligible in both simulations. Recalling equation (1), we conclude that the observed drop in the VV simulation's near-SOL target temperature is a result of ionisation as a particle source rather than ionisation as an energy sink (i.e. an increase in the second term in the denominator of equation (1) rather than a decrease in the second term in the numerator of equation (1)).

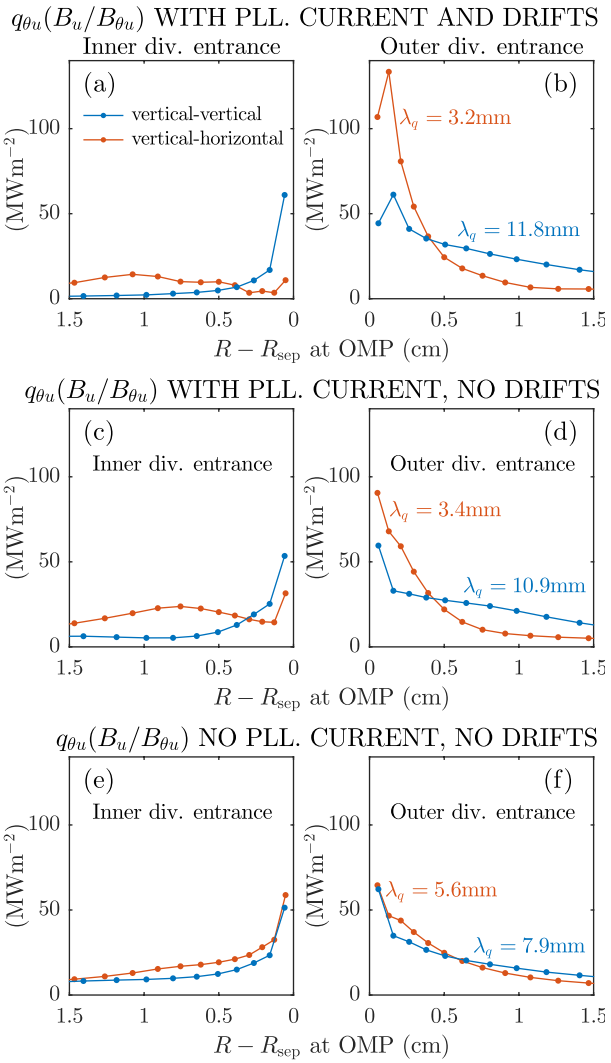

Figure 6. Radial plots of $q_{\theta u}(B_u/B_{\theta u})$ at the inner and outer divertor entrances. (*a*) and (*b*) In the full simulation with drifts and parallel current. (*c*) and (*d*) In a simulation with parallel current but without drifts. (*e*) and (*f*) In a simulation with neither drifts nor parallel current. All three simulations shown are in the steady state.

The total heat sink in figure 8(*a*) is quite similar in both simulations, even though the components of the radial flows are different. In VV, the radial outflux of heat into the PFR due to conduction and drift convection is smaller than in VH. However, this is largely compensated by a higher convected flow associated with the anomalous flux in VV. The result is that the radial divergence of the total radial heat flow is similar in VV and VH simulations, so that the differences in the heat flux density at the target are caused primarily by differences in the heat flux density entering the divertor (which were previously shown in figure 6(*b*)).

Figure 9 plots $q_{\mathrm{dep}}\,(f_R/\cos\phi)$ at the outer target for the VV and VH simulations (the blue line is equal to the sum of the blue lines in figures 6(*b*) and 8(*a*) and the red line is equal to the sum of the red lines in figures 6(*b*) and 8(*a*)). Ignoring effects of different target inclination angles and different total flux expansions (which themselves are quite small), we see that the peak target-deposited heat flux is 2.5 times higher in VH than in VV.

4. Discussion

4.1. The lower tile reflection pathway

To the authors' knowledge, the importance of lower tile reflections in the context of the vertical–vertical divertor configuration has not been previously recognised in the literature. In [10], it was stated that 'in a vertical divertor, the recycling neutrals are emitted towards the separatrix, which becomes a region of preferential ionisation', and that 'for typical parameters at the plasma edge, the ionization mean free path of neutrals recycled at the divertor target is similar (usually shorter) to the typical dimensions of the divertor plasma'. In our simulations, although the separatrix does become a region of preferential ionisation, the primary reason for that is neutral reflection from the lower tiles and subsequent penetration back to the separatrix. In particular, neutrals originating from the inner target (and predominantly reflected from the lower tiles) contribute 44% of the outer separatrix ionisation source. This can only happen in a situation where the PFR is sufficiently transparent to allow neutrals to pass through it (note that this is a necessary but not sufficient condition; the transfer of neutrals between divertors will also depend on the particular geometry employed).

In Vertical–horizontal configuration, the lower tile reflection pathway is strongly attenuated. For neutrals originating from the outer horizontal target, this is a result of neutrals being reflected preferentially into the outer SOL, where they are ionised before reaching the outer wall; for the horizontal target, there is no outer-tile-reflected equivalent to the lower-tile-reflected pathway. For neutrals originating from the inner target, their reduced contribution to the outer divertor ionisation is a result of reduced neutral penetration across the PFR and, to a lesser extent, reduced inner target recylcing flux (itself a result of reduced inner divertor ionisation source due to neutrals originating from the outer target). In the absence of these lower tile reflection pathways, the outer divertor ionisation peaks radially outward from the separatrix as a result of preferential recyling into the SOL.

4.2. Influence of drifts and current on λ_q

In the particular JET VH simulation analysed here, whose $\lambda_q = 3.2$ mm at the divertor entrance is similar to values inferred experimentally in JET H-mode plasmas [5], λ_q is significantly narrowed by the presence of drifts and currents. This is opposite to the VV simulation, whose $\lambda_q = 11.8$ mm at the divertor entrance is broadened by the presence of drifts. Both of these behaviours can be traced back to the differing ionisation patterns in VH and VV.

In VH, the peaking of the divertor ionisation radially outward from the separatrix means that: (i) the outer target electron temperature drops quickly in the radial direction, leading to a strong $E_r \times B$ convective heat flux towards the outer target in a narrow near-SOL region (the width of which is set by the radial distance between the separatrix and the outer-divertor-flux-tube-integrated ionisation peak); (ii) in the same narrow region, the target electron temperature is much

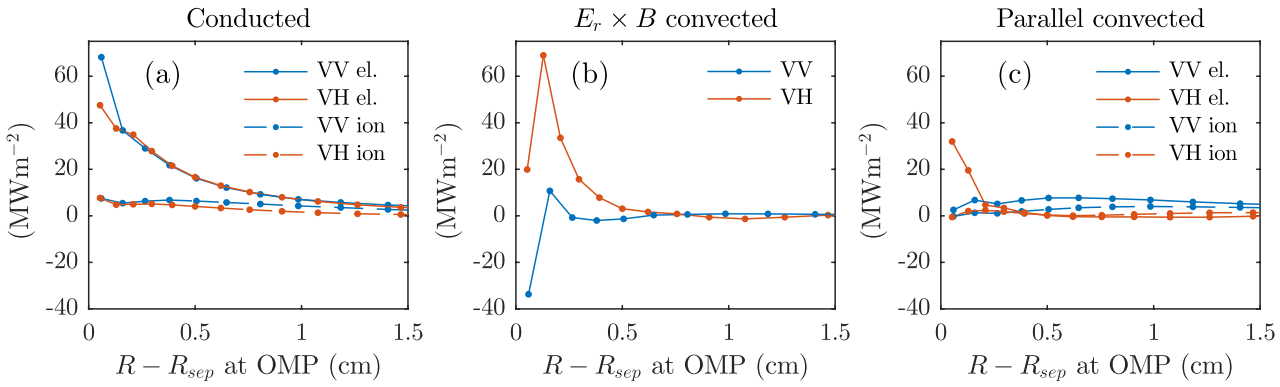

Figure 7. The components of $q_{\theta u}(B_u/B_{\theta u})$ for the default VV and VH simulations, in the presence of drifts and parallel current.

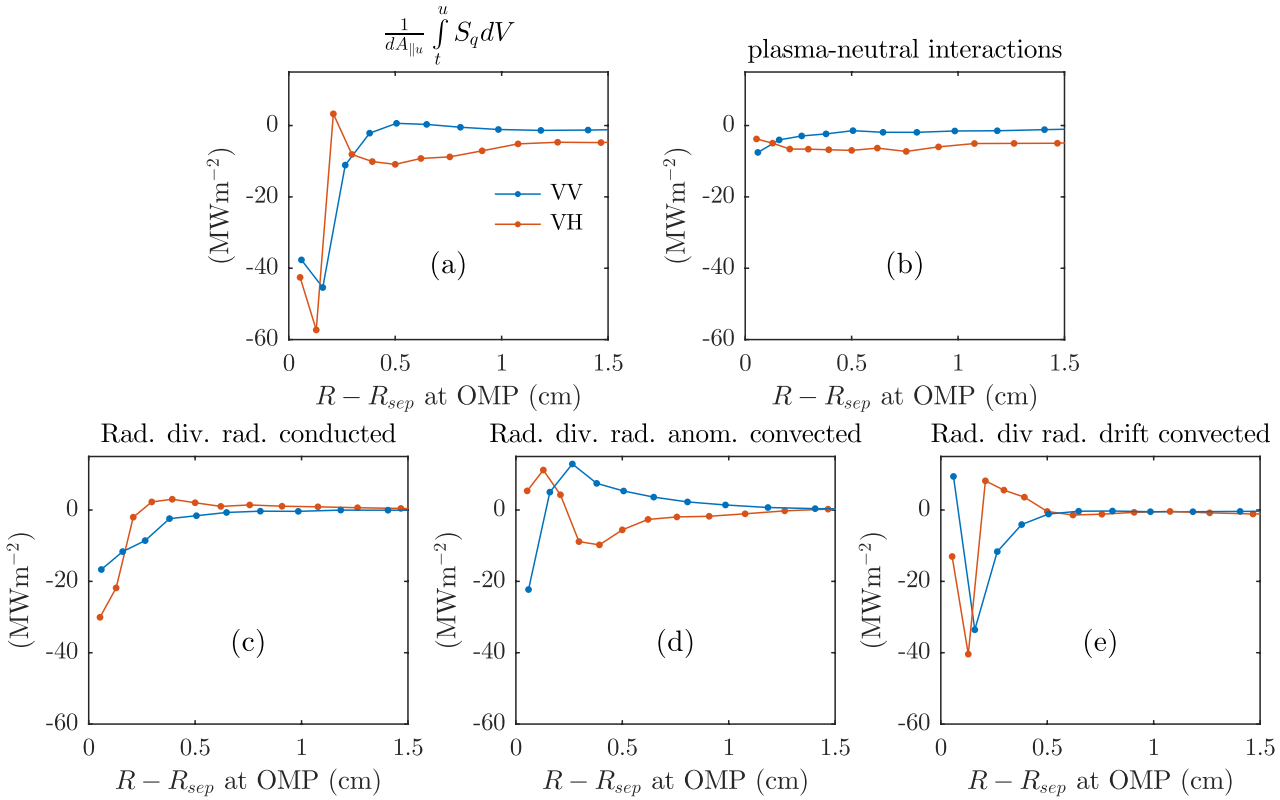

Figure 8. The heat sink in the outer divertor. (*a*) The total heat sink. (*b*)–(*e*) The components of the total heat sink, as labelled in the titles of each axis and discussed in the text.

higher on the outboard side than the inboard side, driving a thermoelectric current towards the inner target and an associated convective electron heat flux towards the outer target. As a result of these two factors, the convective heat flux actually dominates over the conductive heat flux in this narrow region. Critically, the width of this narrow region, i.e. the radial distance between the separatrix and the outer-divertor-flux-tube-integrated ionisation peak, is what sets the outer divertor λ_q in the VH simulation (in figure 1(*e*) we see that this distance (=3.0 mm) is very similar to the fitted $\lambda_q = 3.2$ mm).

By contrast, in the VV simulation, the separatrix-peaked ionisation gives rise to a radially increasing target electron temperature in the near SOL, which leads to an $E_r \times B$ convective heat flow away from the target in that narrow region. This opposes the conducted heat flux entering the outer divertor in the near SOL, flattening out the heat flux density profile and increasing λ_q. Furthermore, there is little thermoelectric current in the VV simulation because the inner and outer target electron temperatures are more similar.

This is an interesting result, with potential (positive) consequences for predictions of λ_q in the ITER vertical–vertical divertor. However, it is somewhat at odds with the widely accepted heuristic model of [8], which has no role for neutrals and which succesfully recovers the $1/B_\theta$ scaling for λ_q observed experimentally [5]. It is not currently clear how one can recover a $1/B_\theta$ scaling in a model where λ_q is set by the radial distance between the separatrix and the outer-divertor-flux-tube-integrated ionisation peak. It is also important to emphasise that these are only two simulations at a specific upstream density and power and for a single device. Future

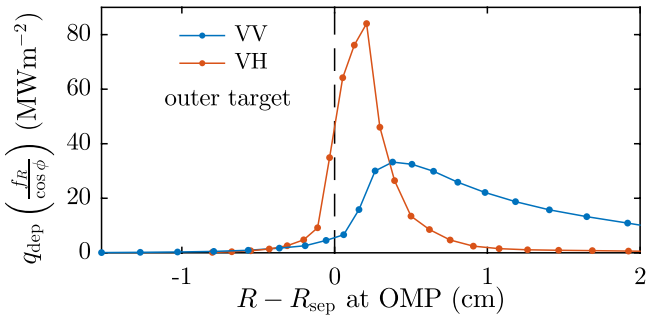

Figure 9. Deposited heat flux at the outer divertor in the VV and VH simulations, without accounting for total flux expansion and target inclination angle.

work should be focused on studying whether such an effect of divertor geometry can be observed in experiment and how the simulated effect changes with simulation parameter scans (of upstream density, power and radial transport). Interestingly in this regard, figure 4 in [6] does appear to indicate a significant (factor 2) increase in the derived λ_q for vertical compared to horizontal targets on ASDEX Upgrade, for experiments in which the plasma current changed only marginally.

From the above reasoning that $E_r \times B$ flows drive a strong convective heat flux, one would predict a significant effect of toroidal magnetic field reversal in a horizontal target configuration. [7] observed little effect on the outer divertor λ_q of reversing the toroidal magnetic field on ASDEX Upgrade. However, the divertor geometry chosen for that experiment was one in which the separatrix was close to normal incidence on the target, so that the ionisation may well have been peaked at the separatrix. This motivates an experimental investigation into the effect of field reversal on λ_q in VH configurations in JET.

5. Conclusions

We draw the following conclusions from this work:

- The radial electric field at the outer midplane of the simulations studied here can be largely attributed to the radial gradient in the outer target electron temperature.
- In the VV simulation the outer target electron temperature peaks at the separatrix while in the VH simulation it peaks radially outward from the separatrix. This is consistent with the fact that the ionisation source peaks at the separatrix in the VV outer divertor and radially outward from the target in the VH outer divertor, as has also been noted in previous works on vertical vs. horizontal target configurations.
- This outer divertor separatrix-peaked ionisation in the VV simulation occurs because neutrals from both targets are preferentially emitted towards the PFR. The transparency of the PFR to those neutrals, combined with reflections from the lower tiles, allows neutrals from both targets (actually to a larger degree from the inner target) to penetrate back to the outer divertor separatrix and ionise there.
- The minimally complex neutral model required to recover the ionisation profile due to neutrals that reflect off the lower tiles is one in which only ionisation and dissociation are included, with realistic tile temperatures and dissociation energies. Interestingly, the molecular speed associated with the tile temperature alone is sufficient for most of the lower-tile-reflected pathway to be activated. This is because most of the lower-tile-reflected neutrals originate from tile regions where the electron temperature is below 5 eV.
- In VH configuration, the outer target emits neutrals into the relatively opaque SOL. The lower tile reflection pathway is therefore strongly reduced, and there is no equivalent outer-tile-reflected pathway to compensate. In addition, the PFR is more opaque to neutrals so that the contribution of inner target neutrals to the outer divertor separatrix ionisation is also strongly reduced. This is the underlying reason why the ionisation source is peaked radially outward from the separatrix in the VH simulation. Simulations of other tokamaks are required to clarify whether this is a JET-specific effect.
- As a result of a strong outer target electron temperature drop, from the separatrix to the position where the outer divertor ionisation peaks, there is a strong convective heat flux towards the target at the divertor entrance in the VH simulation. It is driven by a combination of $E_r \times B$ flow and thermoelectric current, and it is sufficient to dominate over the conductive heat flux in this region. It means that the $\lambda_q = 3.2$ mm at the entrance to the outer divertor in the VH simulation is set by the radial distance between the separatrix and the ionisation peak.
- By contrast, in the VV simulation, the outer target electron temperature is radially increasing in the near SOL. This drives an $E_r \times B$ convective heat flux away from the outer target, opposing the conductive heat flux into the outer divertor entrance, flattening out the heat flux density profile and increasing λ_q, so that $\lambda_q = 11.8$ mm at the outer divertor entrance of the VV simulation.
- The lowered peak heat flux density observed at the outer target in the VV simulation compared to the VH simulation is driven by the lower heat flux density coming into the outer divertor, not by any difference in the heat sink within the divertor volume; the difference in divertor heat sinks is minimal in the two simulations. In particular, the heat sink due to neutrals is negligible in both simulations.

Acknowledgments

The authors would like to thank Alex Chankin for allowing us to use his simulations and to build directly on his work. This work has been carried out within the framework of the EUROfusion Consortium and has received funding from the Euratom research and training programme 2014–2018 under grant agreement No 633053 and from the RCUK Energy Programme [grant number EP/P012450/1]. To obtain further information on the data and models underlying this paper

please contact PublicationsManager@ukaea.uk. The views and opinions expressed herein do not necessarily reflect those of the European Commission.

ORCID iDs

B. Lipschultz https://orcid.org/0000-0001-5968-3684

References

[1] Chankin A.V. *et al* 2017 *Nucl. Mater. Energy* **12** 273
[2] Chankin A.V. *et al* 2001 *J. Nucl. Mater.* **290–3** 518
[3] Chankin A.V. *et al* 2015 *Plasma Phys. Control. Fusion* **57** 095002
[4] Eckstein W. 1991 *Computer Simulation of Ion-Solid Interactions* (Berlin: Springer)
[5] Eich T. *et al* 2013a *Nucl. Fusion* **53** 093031
[6] Eich T. *et al* 2013b *J. Nucl. Mater.* **438** S72
[7] Faitsch M. *et al* 2015 *Plasma Phys. Control. Fusion* **57** 075005
[8] Goldston R.J. 2012 *Nucl. Fusion* **52** 013009
[9] Jaervinen A.E. *et al* 2016 *Plasma Phys. Control. Fusion* **58** 045011
[10] Loarte A. 2001 *Plasma Phys. Control. Fusion* **43** R183
[11] Maggi C.F. *et al* 2014 *Nucl. Fusion* **54** 023007
[12] Reiter D. 1992 *J. Nucl. Mater.* **196–8** 80
[13] Scarabosio A. *et al* 2015 *J. Nucl. Mater.* **463** 49
[14] Simonini R. *et al* 1994 *Contrib. Plasma Phys.* **34** 368
[15] Wiesen S. *et al* 2006 *ITC Proj. Rep.* www.eirene.de/e2deir_report_30jun06.pdf
[16] Litaudon X. *et al* 2017 *Nucl. Fusion* **57** 102001